Journal of Electroanalytical Chemistry 878 (2020) 114539

Contents lists available at ScienceDirect

Journal of Electroanalytical Chemistry

journal homepage: www.elsevier.com/locate/jelechem

The influence of copper and carbon black on electrochemical behavior of nickel positive electrode

Dorcas Zide [a,b,*], Cecil Felix [b], Tobie Oosthuysen [a], Bernard Jan Bladergroen [b]

[a] Department of Chemistry, Cape Peninsula University of Technology, Symphony Way, Bellville, Cape Town 7535, South Africa
[b] South African Institute for Advance Materials Chemistry (SAIAMC), University of the Western Cape, Robert Sobukwe Road, Bellville, Cape Town 7535, South Africa

ARTICLE INFO

Article history:
Received 14 April 2020
Received in revised form 21 July 2020
Accepted 30 July 2020
Available online 3 August 2020

Keywords:
Beta nickel hydroxide
Beta nickel copper hydroxide
Carbon black
Hot-pressed-type
Nickel positive electrode

ABSTRACT

Nickel hydroxide is used as an active material in positive electrodes of secondary alkaline batteries. In alkaline batteries, the capacity of the negative electrode is greater than that of the positive electrode, hence the cell capacity is limited by the positive electrode. The practical capacity of the $Ni(OH)_2$ positive electrode depends on the efficiency of the conductive network connecting the $Ni(OH)_2$ particles with the current collector. In this study, hot-pressed-type electrodes were prepared using fiber-like β-$Ni(OH)_2$ powder as the active material on a nickel mesh as a current collector. The effect of carbon black as a conductive network for $Ni(OH)_2$ active material and the partial substitution of $Cu(OH)_2$ for β-$Ni(OH)_2$ material on the electrode performance, are examined. The carbon black powder addition improves the utilization of the active material; however it lead to a decrease in stability of the electrode. The partial substitution of $Cu(OH)_2$ for β-$Ni(OH)_2$ significantly improves the coulombic efficiency of the β-$Ni(OH)_2$ active material and it also increases the specific discharge capacity and enhance the stability of the electrode. These findings showed that the copper modified β-$Ni(OH)_2$ electrodes possessed an improved specific capacity and stability and thus may be recognized as a promising hybrid material for battery electrode applications.

1. Introduction

Non-renewable sources of energy such as fossil fuels, coal and nuclear fission currently plays a vital role in meeting the economic energy demands of the world [1]. The downside of fossil fuel use is CO_2 emissions, which have been identified as a major global environmental threat owing to its contribution to global warming [2,3]. This has encouraged the development and use of alternative and sustainable renewable energy resources. Two alternatives that have emerged as a suitable solution to upsurge energy security and addressing of environmental issues are wind and solar power [4–6]. The challenge is amplified with the highly concentrated demand peaks in the early morning and early evening when solar generation is minimal. Therefore the energy generated from wind or solar systems is subject to stochastic wind profiles and seasonal availability of resources [7].

Over the years, several energy storage technologies such as mechanical, thermal, and electrochemical energy have been researched. Among the studied electrochemical-based technologies, nickel-iron (NiFe) batteries are commercially viable [8–10]. Yet, there are still several research that hurdles to further enhance its performance which includes poor charging efficiency and low discharge capability [9]. The capacity of the negative electrode is greater than that of the positive electrode and hence the overall poor performance of the NiFe battery is observed [11].

Nickel positive electrode is based on nickel hydroxide ($Ni(OH)_2$) as the active material for storage of electrochemical energy [12–14]. Structurally, two reduction phases, β-$Ni(OH)_2$ and α-$Ni(OH)_2$ and two phases of the oxidized material, β-NiOOH and γ-NiOOH has been reported for the $Ni(OH)_2$ materials [10,15]. The oxidation of β-$Ni(OH)_2$ on charge produces β-NiOOH, on discharge it yields a β-$Ni(OH)_2$ and on overcharge it could be converted to γ-NiOOH. The oxidation of α-$Ni(OH)_2$ on charge produces γ-NiOOH and on discharge it forms an α-$Ni(OH)_2$. In general, α-$Ni(OH)_2$ is unstable and can be transformed to β-$Ni(OH)_2$ in neutral or KOH aqueous solution. Primarily α-$Ni(OH)_2$ is dissolved in the aqueous solution slowly, and then re-nucleated to form β-$Ni(OH)_2$ [16,17]. Owing to the low stability of α-$Ni(OH)_2$ in alkaline media and possibility of battery swelling during charge-discharge, the β-$Ni(OH)_2$ is usually the preferred precursor material used in alkaline batteries [18].

The theoretical specific capacity of β-$Ni(OH)_2$ material in the nickel positive electrode is 289 $mAhg^{-1}$ but in practice the specific capacity of β-$Ni(OH)_2$ material is below the said expected theoretical capacity. The practical capacity of nickel positive electrode depends on the efficiency of the conductive network connecting the β-$Ni(OH)_2$ particles with current collector [11]. Considering the poor conductivity of β-$Ni(OH)_2$ powder, it is advisable to incorporate conductive materials during electrode construction. It is also important to note that the quantity of β-$Ni(OH)_2$ material could

* Corresponding author at: Department of Chemistry, Cape Peninsula University of Technology, Symphony Way, Bellville, Cape Town 7535, South Africa.
E-mail address: zided41@gmail.com. (D. Zide).

http://dx.doi.org/10.1016/j.jelechem.2020.114539

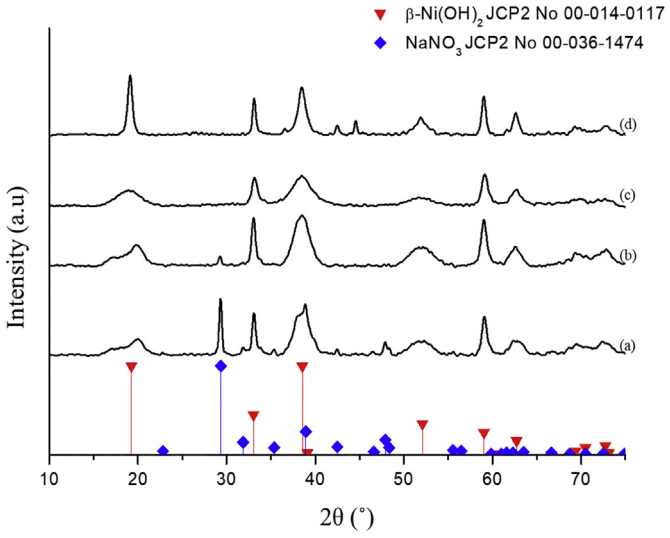

Fig. 1. Diffractograms of the synthesized $Ni(OH)_2$ (a) stirred for 30 min (b) aged for 18 h at room temperature (c) hydrothermal treated for 18 h, and (d) commercial $Ni(OH)_2$.

strongly influence the overall capacity of the electrode. When the β-$Ni(OH)_2$ amount is too high the electrode resistance becomes excessive, which in turn could affect the exploitation of the material and thereby reduces the capacity of the electrode material.

Many studies have revealed that the incorporation of divalent elements such as magnesium, cobalt and zinc can improve active material utilization and cycle life [17,19]. The electrochemical studies of the alpha form of Cu/Ni composition has been reported [20,21]. However, in theory the alpha form of $Ni(OH)_2$ is associated with swelling of the battery during charge-discharge of the battery cell [18].

In the present study the influence of carbon black and the partial substitution of $Cu(OH)_2$ for β-$Ni(OH)_2$ is investigated. The copper is chosen owing to the abundant active sites and synergistic effects between Ni and Cu [22,23]. Ni and Cu are adjacent to one another in the periodic table of elements with atomic numbers 28 and 29 and atomic masses 58.69 amu and 63.55 amu, respectively. To the best of the authors knowledge there are very little work that has been done to assess the effect of carbon black and the partial substitution of $Cu(OH)_2$ for β-$Ni(OH)_2$.

2. Material and methods

2.1. Materials

Sodium carbonate (99%), sodium hydroxide (98%), nickel nitrate hexahydrate, and copper nitrate trihydrate (99%) were purchased from Sigma-Aldrich (South Africa). Carbon black was purchased from Alfa Aesar (United States), coatheylene was purchased from Axalta (United States), and nickel mesh was purchased from Q-Lite batteries (China).

Table 1
Crystallite size of the synthesized $Ni(OH)_2$ stirred for 30 min, aged for 18 h at room temperature, hydrothermal treated for 18 h, and the commercial $Ni(OH)_2$.

	(001)	(101)
Sample name	Crystallite size (nm)	Crystallite size (nm)
30 min mixing: $Ni(OH)_2$	4,05	5,31
18 h ageing: $Ni(OH)_2$	3,88	4,19
18 h hydrothermal: $Ni(OH)_2$	2,59	3,35
Commercial $Ni(OH)_2$	14,36	9,36

Table 2
XRD lattice parameter "a", "c" and "d-spacing" of the commercial and synthesized $Ni(OH)_2$.

Sample name	(001) reflection 2θ (°)	d001 (Å)	(110) reflection 2θ (°)	d110 (Å)	a (Å)	c (Å)
30 min mixing: $Ni(OH)_2$	20,19	4,39	59,11	1,56	3,12	4,39
18 h ageing: $Ni(OH)_2$	20,04	4,43	59,11	1,56	3,12	4,43
18 h hydrothermal: $Ni(OH)_2$	19,21	4,62	59,11	1,56	3,12	4,62
Commercial $Ni(OH)_2$	19,21	4,62	59,11	1,56	3,12	4,62
Standard $Ni(OH)_2$ (JCP2 No 00–041-0117)	19.26	4.60	59.05	1.56	3.13	4.60

2.2. Synthesis of nickel hydroxide active material

The nickel-based active material were prepared using a modified co-precipitation method followed by hydrothermal treatment at pH = 14 [24]. Briefly, two solutions were prepared; solution 1 contained NaOH and Na_2CO_3 and solution 2 contained Ni^{2+} as $Ni(NO_3)_2{\cdot}6H_2O$ salt. The two solutions were mixed dropwise under vigorous stirring at room temperature. The slurry was further agitated at room temperature for 30 min and thereafter subjected to hydrothermal treatment at 65 °C for 18 h. The resulting precipitates were cool at room temperature, then filtered and washed with Milli-Q water. The precipitated samples were dried at 110 °C for 12 h, milled and transferred into vials for later application.

2.3. Synthesis of $Ni_{1-x}Cu_x(OH)_2$ active material

The compositions of $Ni_{1-x}Cu_x(OH)_2$ were prepared using a modified co-precipitation method and followed by hydrothermal treatment at pH = 14 [24]. Where "x" is the weight percentage of Cu^{2+} i.e. 5 wt%, 10 wt%, 25 wt%, and 50 wt%. Briefly, two solutions were prepared; solution 1 contained NaOH and Na_2CO_3 and solution 2 contained Ni^{2+} as $Ni(NO_3)_2{\cdot}6H_2O$ salt, and Cu^{2+} as $Cu(NO_3)_2{\cdot}3H_2O$ salt. The two solutions were mixed dropwise under vigorous stirring at room temperature. The slurry was further agitated at room temperature for 30 min, and thereafter subjected to hydrothermal treatment at 65 °C for 18 h. The resulting precipitates were cool at room temperature, then filtered and washed with Milli-Q water. The precipitated samples were dried at 110 °C for 12 h. The dried powders were crushed and transferred into vials and the samples were labeled as $Ni_{0.95}Cu_{0.05}(OH)_2$, $Ni_{0.9}Cu_{0.1}(OH)_2$, $Ni_{0.75}Cu_{0.25}(OH)_2$, and $Ni_{0.5}Cu_{0.5}(OH)_2$, for the partial substitution of 5 wt% Cu^{2+}, 10 wt% Cu^{2+}, 25 wt% Cu^{2+}, and 50 wt% Cu^{2+}, respectively.

2.4. Structural and morphological characterization of the materials

The diffraction patterns were recorded using a multi-purpose X-ray Diffractometer D8-Advance from BRUKER AXS (Germany). Measurements were operated in a continuous θ - θ scan in locked coupled mode with Cu-Kα radiation ($\lambda K\alpha_1$ = 1.5406 Å) in the 2-theta ranged from 10° to 70°, in steps of 0.034° per second. The functional groups present in the materials were identified using Fourier Transform Infra-red Spectrum II spectrometer (UATR-FTIR, Llantrisant UK), operated using spectrum software; and the absorption bands were collected in the range of 4000 cm^{-1} - 400 cm^{-1}. The thermal analysis was studied using a Perkin-Elmer (6300 instrument) thermal gravimetric analysis (TGA) coupled with differential thermal analysis (TGA-DTA). Measurements were performed under argon gas using a heating rate of 5 °C min^{-1} with a flow rate of 20 ml min^{-1} from 30 °C to 1000 °C temperature range. Their surface areas were analyzed using Brunauer-Emmett-Teller (BET) nitrogen adsorption isotherms and adsorption pore size using Barrett-Joyner-Halenda (BHJ). The compositions were determined using inductively coupled plasma optical

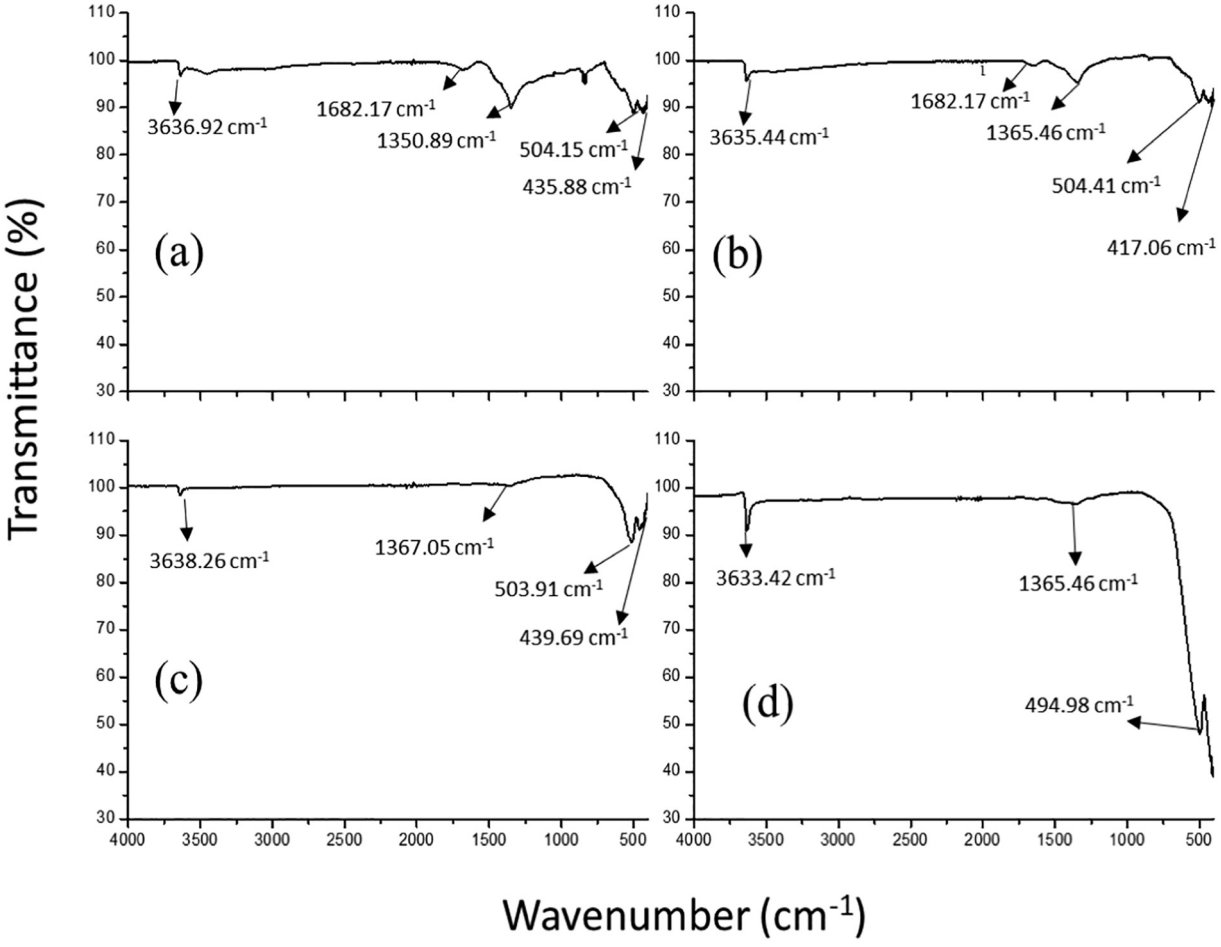

Fig. 2. FTIR spectra of the synthesized $Ni(OH)_2$ (a) stirred for 30 min (b) age for 18 h at room temperature (c) hydrothermal treated for 18 h, and (d) commercial $Ni(OH)_2$.

emission spectroscopy (ICP-OES). The crystal structures of the synthesized materials were confirmed using transmission electron microscopy (TEM).

2.5. Fabrication of electrodes

The nickel electrodes were prepared by mixing 90 wt% active material and 10 wt% coathylene binder thoroughly. The mixture was poured onto a nickel mesh and hot-pressed at 80 °C at 6 MPa using a custom designed hydraulic press for 5 min to assure good electrical contact between the nickel mesh and the active material. Electrode dimensions were kept at 1 cm × 1 cm for all the samples. For further characterization and optimization studies, 85 wt% active material and 5 wt% carbon black, 80 wt% active material and 10 wt% carbon black, and 70 wt% active material and 20 wt% carbon black, respectively were mixed thoroughly with 10 wt% coathylene. Each mixture was dispensed onto a nickel mesh and hot-pressed as mentioned above.

2.6. Electrochemical characterization

The as-prepared nickel electrodes were soaked in 4 M KOH prior to the electrochemical measurements for 2 h. The cyclic voltammetry (CV) was used for identification of redox couples and chrono charge-discharge galvanostatic (CCDG) for capacities of the active materials. Electrochemical characterizations were performed using the Metrohm Auto Lab PGSTAT302N connected to a three-electrode set-up using 4 M KOH as the electrolyte. A graphite sheet (3 cm × 4 cm), and Hg/HgO/4 M KOH were used as counter and reference electrode, respectively.

3. Results and discussion

3.1. Influence of Cu^{2+} on the structure and morphology of the synthesized $Ni(OH)_2$ material

3.1.1. Structural characterization of synthesized $Ni(OH)_2$

The crystalline phase of the synthesized $Ni(OH)_2$ were confirmed using XRD and indexed with the closest fit JCP2 standards. Further compared with the commercial $Ni(OH)_2$ and cross-referenced with published literature. Fig. 1, depicts the diffractogram of the synthesized $Ni(OH)_2$ after 30 min mixing at room temperature (Fig. 1a), aged at room temperature for 18 h (Fig. 1b), hydrothermal treated for 18 h (Fig. 1c), and commercial $Ni(OH)_2$ (Fig. 1d).

The obtained diffractogram in Fig. 1a shows a significant presence of nitratine ($NaNO_3$) (JCP2 No 00–036-1474) at around 29°, 32°, 35°, 42°, 46° and 48°. As the sample was further aged at room temperature for 18 h (Fig. 1b) the presence of $NaNO_3$ were minimal. The peak at 29° started to compact as compared to Fig. 1a, however, it can be noted that the rest of peaks at around 32°, 35°, 42°, 46° and 48° that corresponded to $NaNO_3$ were not present. The double peak bump between 17.189° and 20.189° (Fig. 1a-b) may be owing to the formation of a mixture of $NaNO_3$ (JCP2 No 00–036-1474) and β-$Ni(OH)_2$ (JCP2 No 00–014-0117).

The obtained patterns of the hydrothermal treated $Ni(OH)_2$ (Fig. 1c) were indexed to the pure hexagonal phase of β-$Ni(OH)_2$ standard (JCP2 No 00–014-0117). Similar diffractograms were reported in the literature [12,25,26]. Furthermore, the hydrothermal treated $Ni(OH)_2$ presented in Fig. 1c exhibited no marked significant differences when compared to the observed crystallite of the commercial $Ni(OH)_2$ (Fig. 1d). However, an additional three peaks at 2θ equal to 36.53°, 42.58°, and 44.70° for the

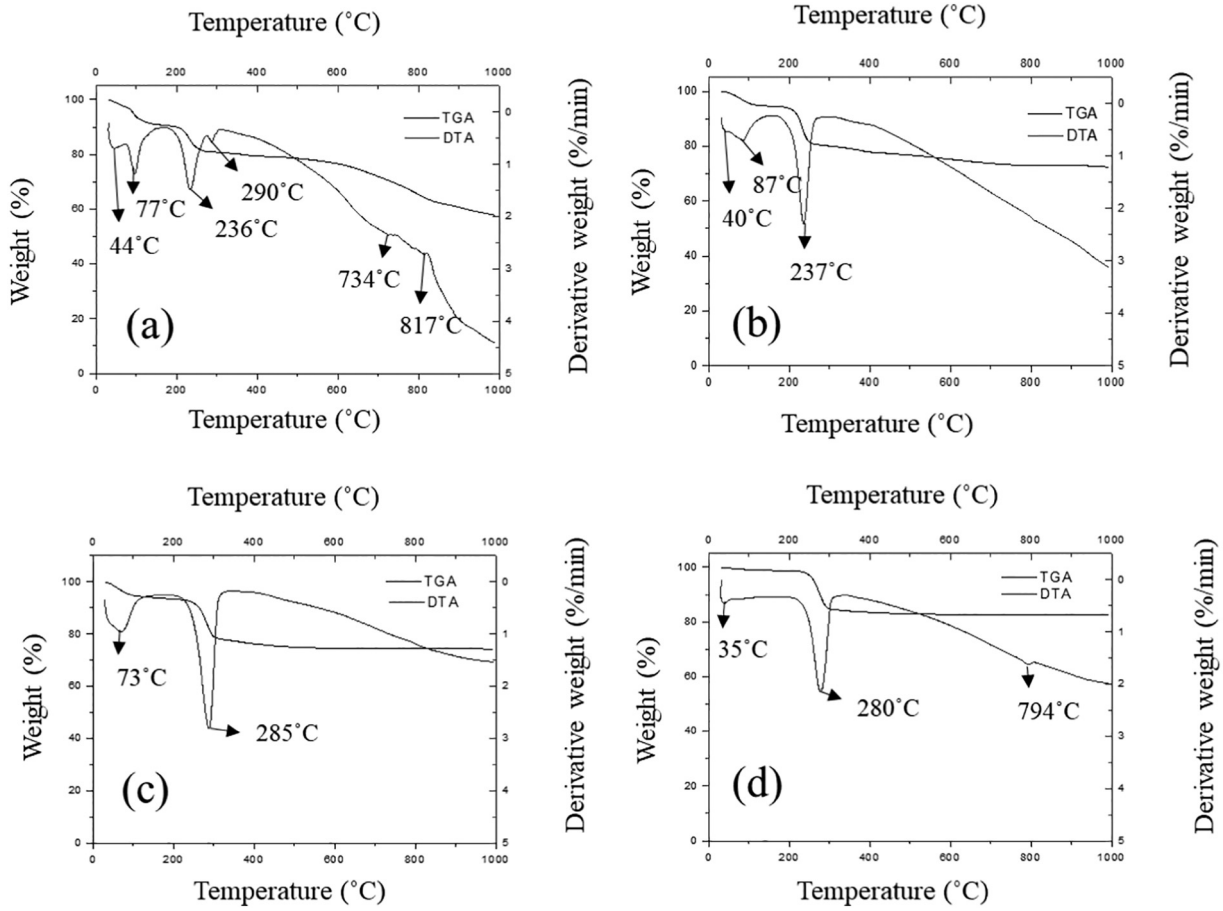

Fig. 3. TG-DTA curves of the synthesized $Ni(OH)_2$ (a) stirred for 30 min (b) age for 18 h at room temperature (c) hydrothermal treated for 18 h, and (d) commercial $Ni(OH)_2$.

commercial $Ni(OH)_2$ were observed. These peaks may be the result of an added modifier, conducting material and/or impurities which were closely fitted to zincite (ZnO) (JCP2 No 00–036-1451), $NaNO_3$ (JCP2 No 00–036-1474) and Ni-metal (JCP2 No 00–004-0850), respectively.

The crystallite sizes of the materials were calculated from the two major peaks (001), and (101) using the Debye-Scherer formula presented in Eq. 1 and the results are shown in Table 1.

Equation 1 Debye-Scherer equation.

$$D = \frac{K\lambda}{\beta Cos\theta}$$

where D is the crystallite size, K is the Scherer constant (K = 0.9), β is the full width of half maximum (FWHM) and θ is the diffraction maximum angle (°). As shown in Table 1, a decrease in crystallite size was observed as the synthesized samples were further treated. The crystallite sizes of the commercial $Ni(OH)_2$ were higher as compared to the synthesized Ni $(OH)_2$ samples.

Table 3
BET surface area and BJH adsorption average pore size of the synthesized $Ni(OH)_2$ after 30 min mixing, 18 h ageing and 18 h hydrothermal treatment and the commercial $Ni(OH)_2$.

Sample name	BET surface area (m^2/g)	Pore size (nm)
30 min mixing: $Ni(OH)_2$	8.74	22.12
18 h ageing: $Ni(OH)_2$	44.48	11.62
18 h hydrothermal: $Ni(OH)_2$	361.92	6.29
Commercial $Ni(OH)_2$	9.27	14.66

The unit cell parameters "a" and "c" were calculated using the formulae $a = 2d_{110}$, and $c = d_{001}$; where d_{001} and d_{110} are the basal spacing at a miller indices (hkl) of (001) and (110) which were obtained using Bragg's law equation (Eq. 2), assuming hexagonal stacking [27]. The obtained results are presented in Table 2.

Equation 2: Bragg's law

$$n\lambda = 2d\ \sin\theta$$

where n is the order number, λ is the wavelength (1.54098 Å), d is the basal spacing (Å) and θ is the diffraction angle (°). As presented in Table 2, the lattice parameter "a" for all the synthesized samples (Fig. 1a-c) were the same (3.12Å). However, the parameter, "c" increases as samples were further treated with the calculated c-parameters of 4.39Å, 4.43Å, and 4.62Å, respectively. It can be noted that the hydrothermal treated sample had the same "a"-parameter and "c"-parameter values as the commercial $Ni(OH)_2$ ($a = 3.12$Å, $c = d_{001} = 4{,}62$ Å), which both corresponded to the β-Ni $(OH)_2$ (JCP2 No 00–014-0117).

Fig. 2 depicts the FTIR spectra of the synthesized samples. The presence of sharp peaks at around 3636.92 cm^{-1}, 3635.33 cm^{-1}, 3638.26 cm^{-1} and 3633.42 cm^{-1} in Fig. 2(a-d), respectively is the confirmation of $Ni(OH)_2$ [28,29]. These absorption bands are assigned to O—H stretching vibrations [11,12,28,30]. The peaks at around 1682.17 cm^{-1} on both the synthesized $Ni(OH)_2$ stirred for 30 min (Fig. 2a) and aged for 18 h at room temperature (Fig. 2b), is attributed to the bending vibration mode of H_2O molecules. The absorption bands at around 1300 cm^{-1}, 500 cm^{-1} and 400 cm^{-1} in Fig. 2 (a-d) are attributed to the existence of interlayer nitrate anions (NO^-_3), Ni—O stretching vibrations and an in-plane Ni-O-H bending vibration respectively [11,12,28,30].

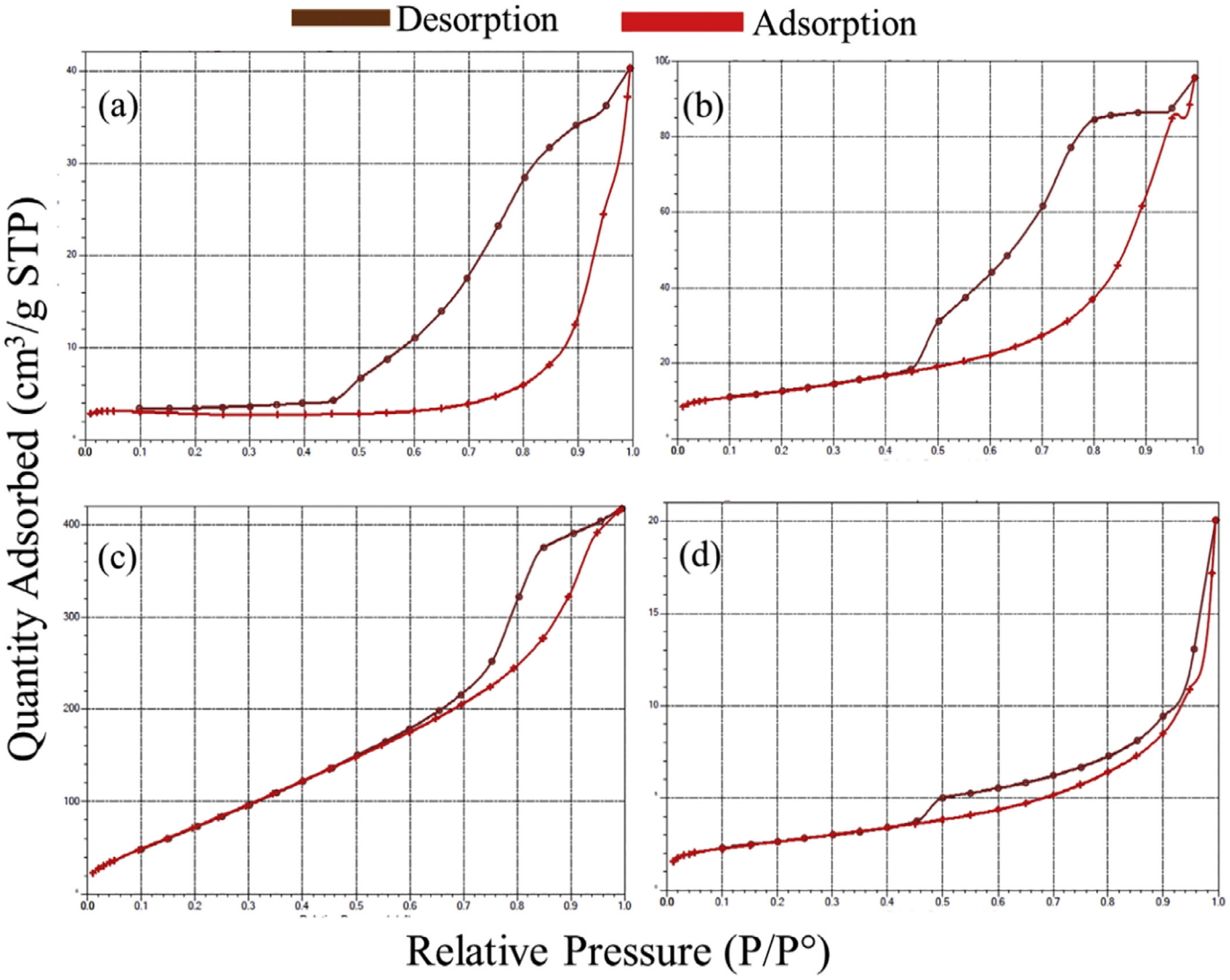

Fig. 4. Nitrogen adsorption – desorption isotherm of the synthesized $Ni(OH)_2$ (a) stirred for 30 min (b) age for 18 h at room temperature (c) hydrothermal treated for 18 h, and (d) commercial $Ni(OH)_2$.

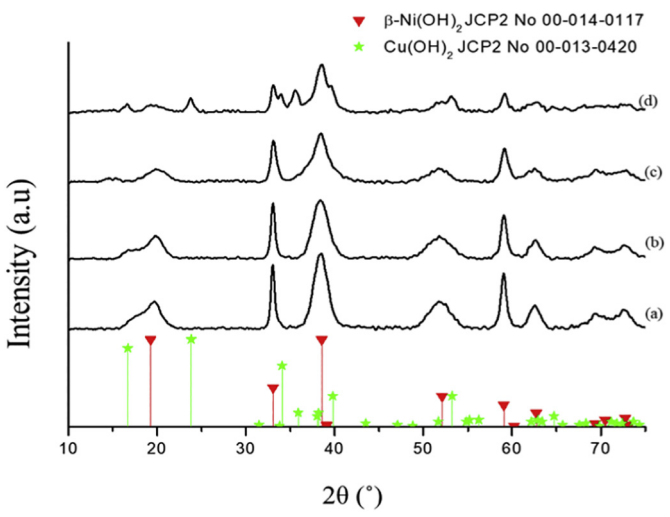

Fig. 5. Diffractograms of (a) $Ni_{0.95}Cu_{0.05}(OH)_2$, (b) $Ni_{0.9}Cu_{0.1}(OH)_2$ (c) $Ni_{0.75}Cu_{0.25}(OH)_2$, and (d) $Ni_{0.5}Cu_{0.5}(OH)_2$.

Fig. 3 shows the thermal behavior of the synthesized $Ni(OH)_2$ samples. The DTA curve of the synthesized $Ni(OH)_2$ stirred for 30 min (Fig. 3a) showed six exothermic peaks with temperatures at 44 °C, 77 °C, 236 °C, 290 °C, 734 °C and 817 °C indicating continuous degradation of the sample and continuous sample mass loss. The first two peaks (44 °C and 77 °C) may be due to the evaporation of residual water in the dried sample [28] resulting to the initial weight loss of 9.59% (TGA curve). The other sharp peak located at 236 °C (DTA curve) may be the indicative of the removal of OH group during the transformation of $Ni(OH)_2$ to NiO [28,31], resulting to a second weight loss of 8.32%. A gradual weight loss of 3.29% between 230 °C and 290 °C was observed, which may be owing to crystallization within the sample. This loss continues at a slow rate up to 734 °C to yield another weight loss of 15.77% and further 5.43% at 817 °C.

Fig. 3b showed three exothermic peaks with temperatures at 40 °C, 87 °C and 237 °C. The first two peaks (40 °C and 87 °C) may be due to the evaporation of residual water in the dried sample [28], resulting in the initial weight loss of 5.0%. The other sharp peak located at 237 °C may be indicative of the removal of an OH^- group during the transformation of Ni $(OH)_2$ to NiO [28,31], corresponding to a total weight loss of 13.28% followed by a weight loss of 8.32% that may be due to structural changes within the sample. It can be noted that the sample showed less reduction as compared to the sample presented in Fig. 3a.

O-H bond ~ 3600 cm^{-1} , **H_2O molecules** ~ 1600 cm^{-1}, **SO^{2-}_4** or **NO^-_3** ~ 1300 cm^{-1} , **Ni-O stretching** ~600 cm^{-1}, and **in-plane Ni-O-H bending vibration** ~400 cm^{-1} [12].

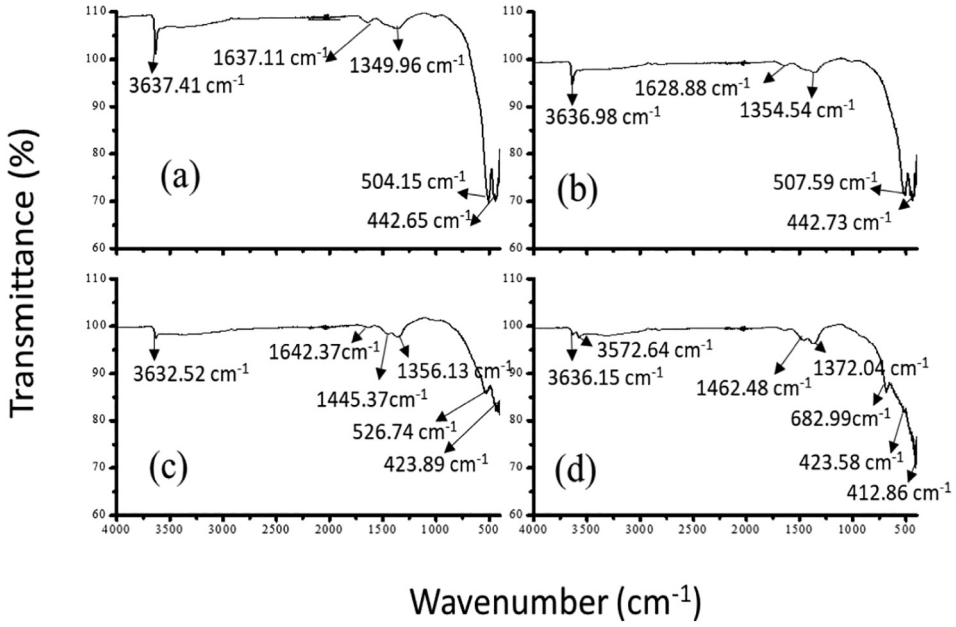

Fig. 6. FTIR spectra of (a) $Ni_{0.95}Cu_{0.05}(OH)_2$, (b) $Ni_{0.9}Cu_{0.1}(OH)_2$, (c) $Ni_{0.75}Cu_{0.25}(OH)_2$, and (d) $Ni_{0.5}Cu_{0.5}(OH)_2$.

Only two weight losses at 73 °C and 285 °C corresponding to weight losses of 5.20% and 8.32%, respectively were observed on the hydrothermal treated sample (Fig. 3c). These weight losses may be due to the evaporation of residual water in the dried sample [28] and decomposition of Ni $(OH)_2$ to NiO, respectively [28,31]. A further weight loss of 3.94% due to structural changes within the sample was observed.

Fig. 3d showed a small peak at 35 °C resulting in a weight loss of 0.87%. A radical weight loss of 14.09% was observed at 280 °C and as the sample slowly crystallized, a weight loss of 1.27% was calculated followed by a further weight loss of 0.8% corresponding to a small peak at 794 °C was obtained. The thermal behavior of $Ni(OH)_2$ based material using TG-DTA has been reported in the literature. Shanaj and John [28], reported three weight losses corresponding to DTA curves at 55 °C, 89 °C and 290 °C. The general proposed thermal dehydration and decomposition reactions are presented in Eq. 3 and Eq. 4 respectively.

Equation 3: Thermal dehydration composition reaction of $Ni(OH)_2$

$$Ni(OH)_2 \cdot xH_2O \rightarrow Ni(OH)_2 + xH_2O$$

Equation 4: Thermal decomposition reaction of $Ni(OH)_2$

$$Ni(OH)_2 \xrightarrow{300^{\circ}C} NiO + H_2O$$

The Brunauer-Emmett-Teller (BET) specific surface areas (Table 3) increase as further treatments were performed. A lower surface area of 8.74 m^2/g and 44.48 m^2/g for the synthesized $Ni(OH)_2$ stirred for 30 min and $Ni(OH)_2$ aged for 18 h at room temperature, respectively were observed. While the BET surface area of the commercial $Ni(OH)_2$ was found to be 9.27m^2/g. Such lower surface areas have been reported [32,33]. The hydrothermal treated sample demonstrated a higher surface area (361.92 m^2/g) and this finding corresponded with the BET specific surface area of $Ni(OH)_2$ (384 m^2/g and 343 m^2/g) reported in literature [34].

The average pore size distribution obtained from the adsorption branch of the isotherms by the Barrett-Joyner-Halenda (BJH) method (Table 3) further confirms a mesoporous structure within a size range of 6–22 nm. As shown in Table 3, the average pore sizes of the synthesized samples decreases as the sample were further subjected to treatment.

The nitrogen adsorption – desorption isotherms of the synthesized Ni $(OH)_2$ and the commercial $Ni(OH)_2$ are presented in Fig. 4. The samples can be classified as type IV isotherm with a distinct hysteresis loop, indicating the presence of mesoporous structures at the relative pressure (P/P°) range between 0.48 and 1.0 (Fig. 4a, b, d) and 0.7 and 1.0 (Fig. 4c), which could be revealing the presence of mesoporous characteristics. These findings were in agreement with the results reported in literature [35–37].

3.1.2. Structural characterization of $Ni_{1-x}Cu_x(OH)_2$

The obtained XRD patterns of $Ni_{1-x}Cu_x(OH)_2$ composition (where x is equal to 5 wt%, 10 wt%, 25 wt%, and 50 wt%) are reported in Fig. 5(a-d). Common peaks in the diffractograms of $Ni_{0.95}Cu_{0.05}(OH)_2$ (Fig. 5a), $Ni_{0.9}Cu_{0.1}(OH)_2$ (Fig. 5b), $Ni_{0.75}Cu_{0.25}$ $(OH)_2$ (Fig. 5c) and $Ni_{0.5}Cu_{0.5}$ $(OH)_2$ (Fig. 5d) at diffraction angles 32.964°, 38.43°, 51.769°, and 59.106°, were observed. These peaks corresponded to $Ni(OH)_2$ (JCP2 No 00–014-0117) and $Cu(OH)_2$ (JCP2 No 00–013-0420).

The calculated crystallite sizes using Debye-Scherer formula (Eq. 1) from the two major peaks, (001) and (101) index, ranged from 2 nm to 3 nm depending on the sample composition. Furthermore, the calculated unit cell parameters "a" were found to be 3.124Å for all the diffractograms presented in Fig. 5a-d and this value was in agreement with the JCP2 No 00–014-0117 standard $Ni(OH)_2$ (3.126Å). The lattice constant, "c" increases with increase in Cu^{2+} addition, 4.460Å (Fig. 5a-b), 4.486Å (Fig. 5c), and 4.582Å (Fig. 5d). This may be signifying the presence of foreign atoms at the Ni lattice points, which may be either larger or smaller than the host atom (Ni).

Fig. 6, depicts the FTIR spectra of the as-prepared samples. The O—H bond was observed at around 3638.12 cm^{-1}, 3637.43 cm^{-1}, 3633.58 cm^{-1} and 3571.96 cm^{-1} for Fig. 6a-d, respectively. It can be noted that the bands slightly shifted to a lower wavenumber as the amount of copper substituent was increased during the synthesis. Furthermore, absorption bands due to NO^-_3 anion were observed at a wavenumber of

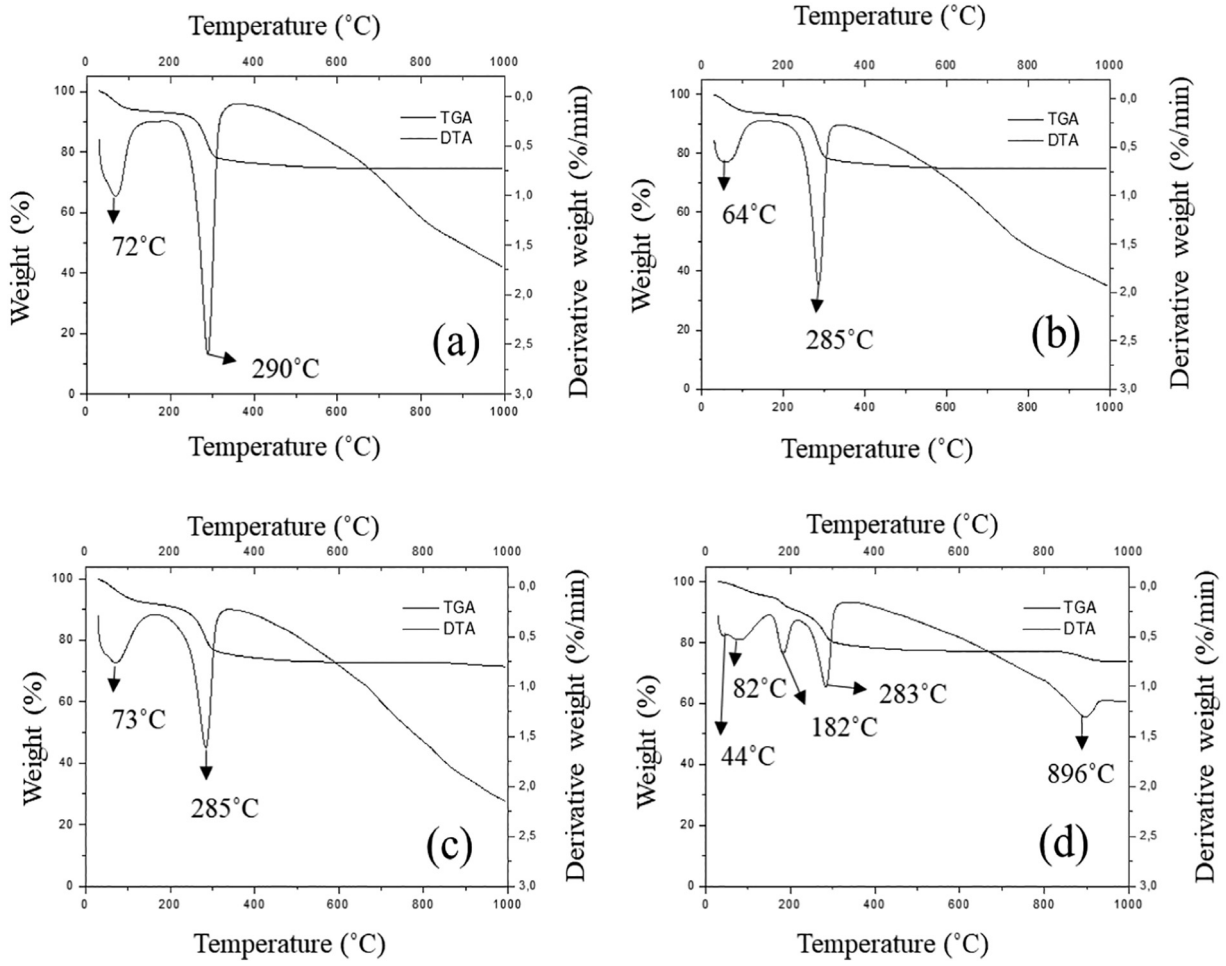

Fig. 7. TG - DTA) curves of (a) $Ni_{0.95}Cu_{0.05}(OH)_2$, (b) $Ni_{0.9}Cu_{0.1}(OH)_2$ (c) $Ni_{0.75}Cu_{0.25}(OH)_2$, and (d) $Ni_{0.5}Cu_{0.5}(OH)_2$.

Table 4
BET specific surface area and elemental composition ratio of $Ni_{1-x}Cu_x(OH)_2$.

Sample name	BET surface area (m^2/g)	Pore size (nm)	Expected Ni^{2+}:Cu^{2+}	ICP-OES Ni^{2+}:Cu^{2+}	SEM-EDS Ni^{2+}:Cu^{2+}
$Ni_{0.95}Cu_{0.05(}OH)_2$	129.688	11.370	0.95: 0.05	0.95: 0.05	0.94: 0.06
$Ni_{0.9}Cu_{0.1}(OH)_2$	130.064	9.125	0.90: 0.10	0.90: 0.10	0.89: 0.11
$Ni_{0.75}Cu_{0.25}(OH)_2$	119.073	7.666	0.75:0.25	0.75:0.25	0.74: 0.26
$Ni_{0.5}Cu_{0.\ 5}(OH)_2$	119.076	13.198	0.50: 0.50	0.52: 0.48	0.47:0.53

1349.96 cm^{-1} (Fig. 6a), 1354.54 cm^{-1} (Fig. 6b), 1356.13 cm^{-1} (Fig. 6c) and 1372.04 cm^{-1}(Fig. 6d), respectively.

The thermal behavior of $Ni_{1-x}Cu_x(OH)_2$ were also investigated and the obtained TG-DTA curves are presented in Fig. 7. Fig. 7a-c demonstrates two distinct weight losses; the initial weight losses of 7.12 wt% (Fig. 7a), 6.5 wt% (Fig. 7b) and 8.37 wt% (Fig. 7c) corresponded to small endothermic peaks at 72 °C, 64 °C and 73 °C respectively. The melting point of Cu $(OH)_2$ and $Ni(OH)_2$ are expected to occur at 80 °C and 230 °C, respectively. In general the degradation of the dried sample is expected to occur before its melting point [12]. It can be said that these initial weight losses are due to evaporation of residual water in the dried $Ni_{1-x}Cu_x(OH)_2$ samples. The second sharp peaks located at 290 °C, 285 °C and 285 °C corresponding to a weight losses of 18.41 wt% (Fig. 7a), 18.22 wt% (Fig. 7b) and 20.15 wt % (Fig. 7c), respectively may be related to the thermo oxidative decomposition of $Ni_{1-x}Cu_x(OH)_2$.

It could be noted that Fig. 7d demonstrated that the sample underwent five distinct weight losses corresponding to 44 °C, 82 °C, 182 °C, 283 °C and 896 °C. These observations were similar to that reported in the literature [38].

The BET surface areas ranged between 130 m^2/g to 119 m^2/g and the BHJ average pore size adsorption ranged from 7.666 nm to 11.370 nm (Table 4). The elemental composition confirmed using ICP and SEM/EDS were in agreement with the intended compositions of $Ni_{0.95}Cu_{0.05}(OH)_2$, $Ni_{0.9}Cu_{0.1}(OH)_2$, $Ni_{0.75}Cu_{0.25}(OH)_2$ and $Ni_{0.5}Cu_{0.5}(OH)_2$ (Table 4).

Fig. 8, shows the nitrogen adsorption – desorption isotherm of the synthesized $Ni_{1-x}Cu_x(OH)_2$, which could be classified as type IV isotherm with a distinct hysteresis loop, indicating the presence of mesoporous structures at the relative pressure (P/P^o) range between 0.5and 1.0 (Fig. 8a-d). These findings were in agreement with the results reported in literature [35–37].

3.1.3. Morphological characterization of synthesized $Ni(OH)_2$ and $Ni_{0.75}Cu_{0.25}(OH)_2$

Fig. 9 demonstrates the TEM images of the charged state and the discharged state of both synthesized $Ni(OH)_2$ and $Ni_{0.75}Cu_{0.25}(OH)_2$ after 20 cycles, compared to their pure materials before hot pressing and after hot pressing. Morphological changes of the synthesized $Ni(OH)_2$ was observed after hot pressing as compared to pure powdered form before hot

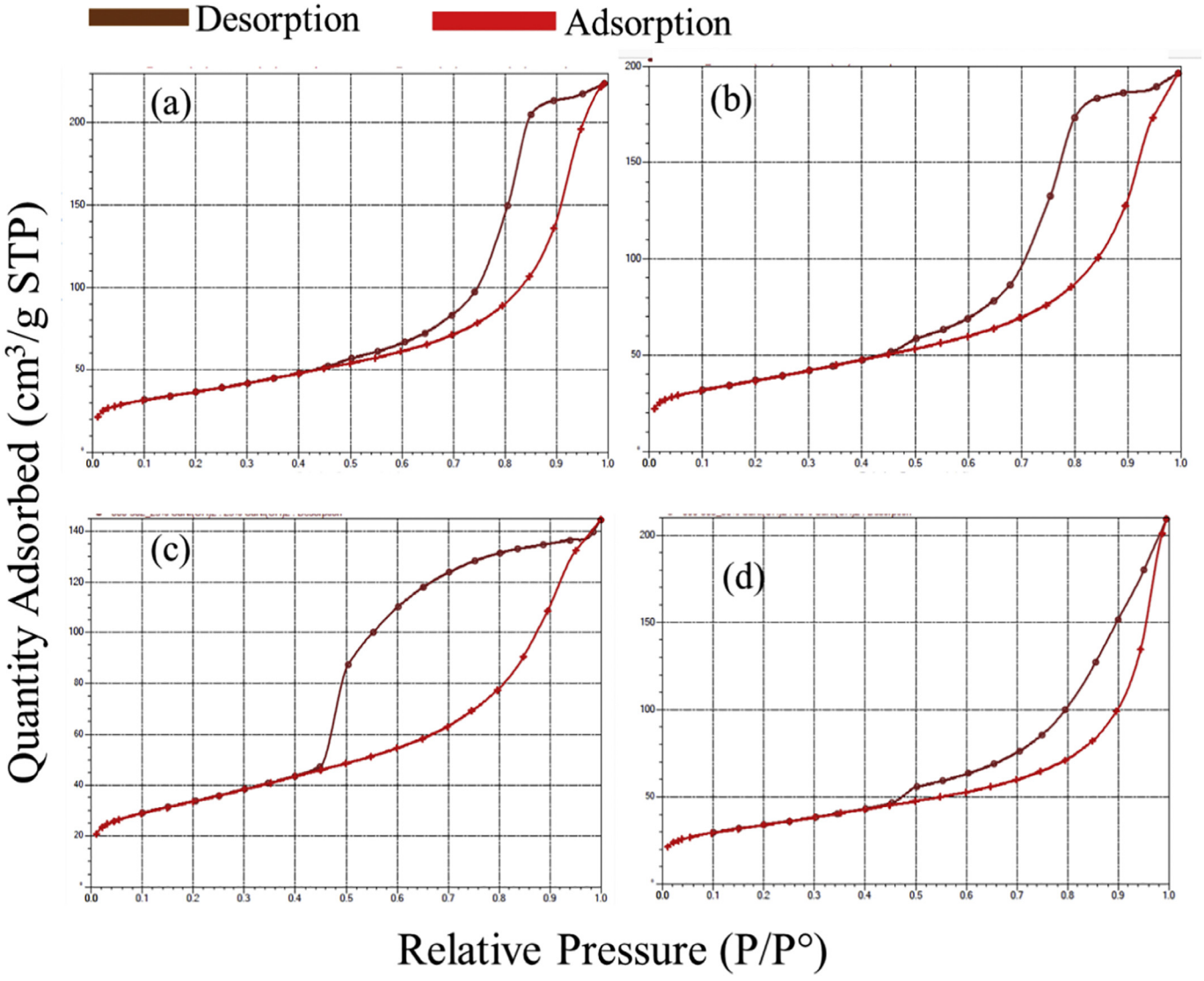

Fig. 8. Nitrogen adsorption – desorption isotherm of the (a) $Ni_{0.95}Cu_{0.05}(OH)_2$, (b) $Ni_{0.9}Cu_{0.1}(OH)_2$ (c) $Ni_{0.75}Cu_{0.25}(OH)_2$, and (d) $Ni_{0.5}Cu_{0.5}(OH)_2$.

pressing (Fig. 9a,b). Although structural changes of the charge states on the synthesized $Ni(OH)_2$ (Fig. 9c) was observed it could be noted that the discharged states (Fig. 9d) was similar to the observed morphology after hot pressing (Fig. 9b). This could be an indication of the good reversibility of the active materials. A similar trend was observed for the $Ni_{0.75}Cu_{0.25}(OH)_2$ active material (Fig. 9e-f).

3.2. Influence of Cu^{2+} on electrochemical performance of electrode

3.2.1. Cyclic voltammetry of the synthesized $Ni(OH)_2$ and $Ni_{0.75}Cu_{0.25}(OH)_2$

Fig. 10a shows the cyclic voltammograms (CVs) of the synthesized Ni $(OH)_2$ with and without carbon black, compared to the commercial Ni $(OH)_2$. There is no difference observed between the synthesized $Ni(OH)_2$ and the commercial $Ni(OH)_2$; the results demonstrated a broad oxidation and reduction potential peaks for all the CVs presented. The broad peaks may be indicative of the capacitive nature of the material where capacitive current overlaps with Faradiac current or a result of a diffusion limited process.

It can be noted that $Ni_{0.75}Cu_{0.25}(OH)_2$ (Fig. 10b) also showed the broad oxidation-reduction potential peaks thus the incorporation of copper and the addition of carbon black did not affect the electrochemical redox reactions of the $Ni(OH)_2$. However, from Fig. 8c it can be noted that the oxidation of copper occurs at negative potentials and that the addition of carbon black promotes the oxidation of copper. At −0.4 V, a small anodic peak is observed corresponding to the formation of the Cu $(OH)_2$ species while at −0.14 V the $Cu(OH)_2$ species are oxidized to form Cu_2O [22].

Although both oxidation and reduction peaks (Fig. 10a-b) were broader, their appearance in the approximately same potential window is indicative of good reversibility of the active materials. These finding are in agreement with the TEM images which showed good reversibility as indicated by similar structural appearance of the hot-pressed electrode ((Fig. 9b,f) and discharged electrode (Fig. 9d,h).

3.2.2. Optimization of Cu^{2+} substitution to $Ni(OH)_2$

The electrodes were prepared using the synthesized $Ni_{1-x}Cu_x(OH)_2$ (where x is 5 wt%, 10 wt%, 25 wt%, 50 wt%) and the specific discharged capacities were calculated from the chrono charge discharge galvanostatic (CCDG) curves using Eq. 5. The plots of the calculated specific discharge capacities over 20 cycles are presented in Fig. 11.

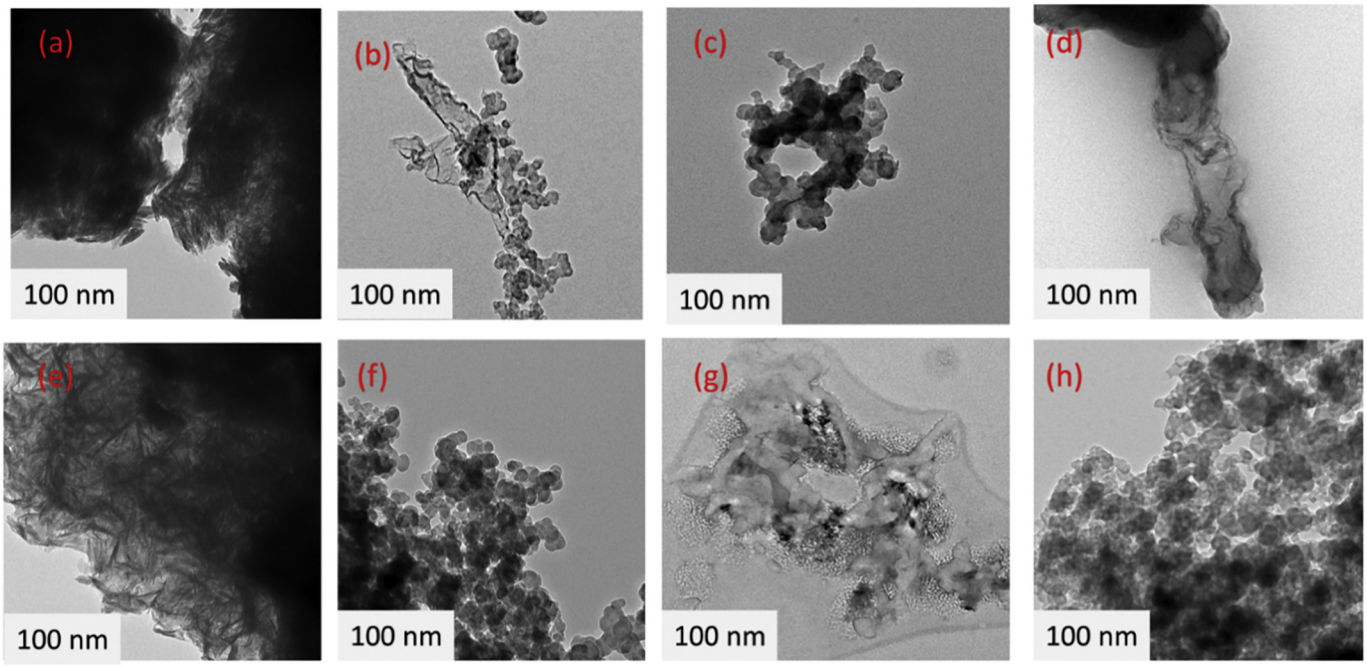

Fig. 9. TEM images of (a) Pure $Ni(OH)_2$ before hot pressing, (b) 85% $Ni(OH)_2$ with 5% carbon black and 10% coathylene after hot pressing (c) Charge state of 85% $Ni(OH)_2$ with 5% carbon black and 10% coathylene after the 20 cycles charge-discharge (d) Discharge state of 85% $Ni(OH)_2$ with 5% carbon black and 10% coathylene after the 20 cycles charge-discharge, (e) Pure $Ni_{0.75}Cu_{0.25}$ $(OH)_2$ before hot pressing, (f) 85% $Ni_{0.75}Cu_{0.25}$ $(OH)_2$ with 5% carbon black and 10% coathylene after hot pressing (g) Charge state of 85% $Ni_{0.75}Cu_{0.25}$ $(OH)_2$ with 5% carbon black and 10% coathylene after the 20 cycles charge-discharge (h) Discharge state of $Ni_{0.75}Cu_{0.25}$ $(OH)_2$ with 5% carbon black and 10% coathylene after the 20 cycles charge-discharge.

Equation 5 Specific discharge capacity formula

$$Specific\ discharge\ capacity = \frac{Applied\ current\ (mA) x\ Discharge\ time\ (h)}{Loading\ mass\ (g)\ of\ the\ active\ material}$$

It can be seen in Fig. 11 that there was no reduction in specific discharge capacities observed over the 20 cycles for 5%wt., 10%wt., and 25%wt copper substitution. The specific discharge capacity for the substitution of 50 wt% copper weight percentage decreased slightly after 12 cycles.

Table 5, presents the calculated specific discharge capacities of 5%wt., 10%wt., 25%wt., and 50 wt% copper substitution for $Ni(OH)_2$ at 20th cycles. As shown in Table 5, the discharge capacity of 169 $mAhg^{-1}$ at 20 cycles was obtained when 25 wt% Cu^{2+} was partial substituted for $Ni(OH)_2$ and appeared to exhibit the optimal composition.

3.2.3. Stability testing of the synthesized $Ni(OH)_2$ and $Ni_{0.75}Cu_{0.25}(OH)_2$

Fig. 12 presents the specific discharge capacities of the synthesized $Ni(OH)_2$ and $Ni_{0.75}Cu_{0.25}(OH)_2$ active materials after 80 cycles and Table 6, depicts the their calculated specific discharge capacities over 80 cycles. The results are compared with the commercial $Ni(OH)_2$ electrode. The electrode of the synthesized $Ni(OH)_2$ without the addition of carbon black showed a reduction of only 18% decrease after the 80th cycle (Fig. 12a), when compared to the electrode with the addition of 5 wt% carbon black, which demonstrated a 66% decrease in discharge capacity after 80 cycles (Fig. 12b).

Both the commercial $Ni(OH)_2$ electrode (Fig. 12c) and $Ni_{0.75}Cu_{0.25}(OH)_2$ electrode (Fig. 12d) showed no reduction after 80 cycles. However, the $Ni_{0.75}Cu_{0.25}(OH)_2$ electrode (Fig. 12d) demonstrated a drastically improved capacity (39% higher than of the commercial $Ni(OH)_2$ electrode) and stability with a specific discharge capacity of 151$mAhg^{-1}$ after 80 cycles. It can also be said that copper stabilized the synthesized $Ni(OH)_2$ resulting in a specific discharge capacity of 151 $mAhg^{-1}$ after the 80th cycle as compared to 51 $mAhg^{-1}$ and 92 $mAhg^{-1}$ (Table 6) for the unmodified $Ni(OH)_2$ and the commercial $Ni(OH)_2$, respectively.

Table 7 illustrates the specific charge and discharge capacities of the synthesized $Ni(OH)_2$ and $Ni_{0.75}Cu_{0.25}(OH)_2$ active materials and their coulombic efficiencies measured at different currents (10 mA, 25 mA, 50 mA, and 75 mA). A coulombic efficiency of 76% was achieved when a current of 10 mA was applied as compared to when currents of 25 mA, 50 mA and 75 mA were applied, where a coulombic efficiencies of 25%, 14% and 10% were obtained, respectively. These results show that the synthesized $Ni(OH)_2$ may operate better at lower currents. The $Ni_{0.75}Cu_{0.25}(OH)_2$ can be applied in both low current and higher current applications. This is evident by higher coulombic efficiencies of 86% at 10 mA and 72% at 25 mA and 55% at 50 mA.

3.3. Effect of carbon black with different weight percentages (0 wt%, 5 wt%, 10 wt%, and 20 wt%) on the electrochemical performance of electrode

Different weight percentages of carbon black (i.e. 0 wt% 5 wt%, 10 wt%, and 20 wt%) were assessed and the attained results were compared with 0 wt% of carbon black (active material without a carbon black). The electrodes were prepared using the synthesized $Ni(OH)_2$ and $Ni_{0.95}Cu_{0.05}(OH)_2$ and the specific discharged capacities were calculated from the CCDG curves using Eq. 5. The prepared electrodes were cycled 20 time at 25 mA and the plotted graphs are shown in Fig. 13 and Fig. 14. The calculated specific discharge capacities at 20th cycles are presented in Table 8.

As shown in Fig. 13 and Table 8 the discharge capacity of 45$mAhg^{-1}$ resulting to a coulombic efficiency of only 30% was obtained for $Ni(OH)_2$ after 20 cycles when carbon black was not added. Mixing 5 wt% carbon black into the electrochemically active material lead to an increase of capacity and coulombic efficiency to 128$mAhg^{-1}$ and 87% respectively. The specific discharge capacity and coulombic efficiencies decreases as more carbon black was

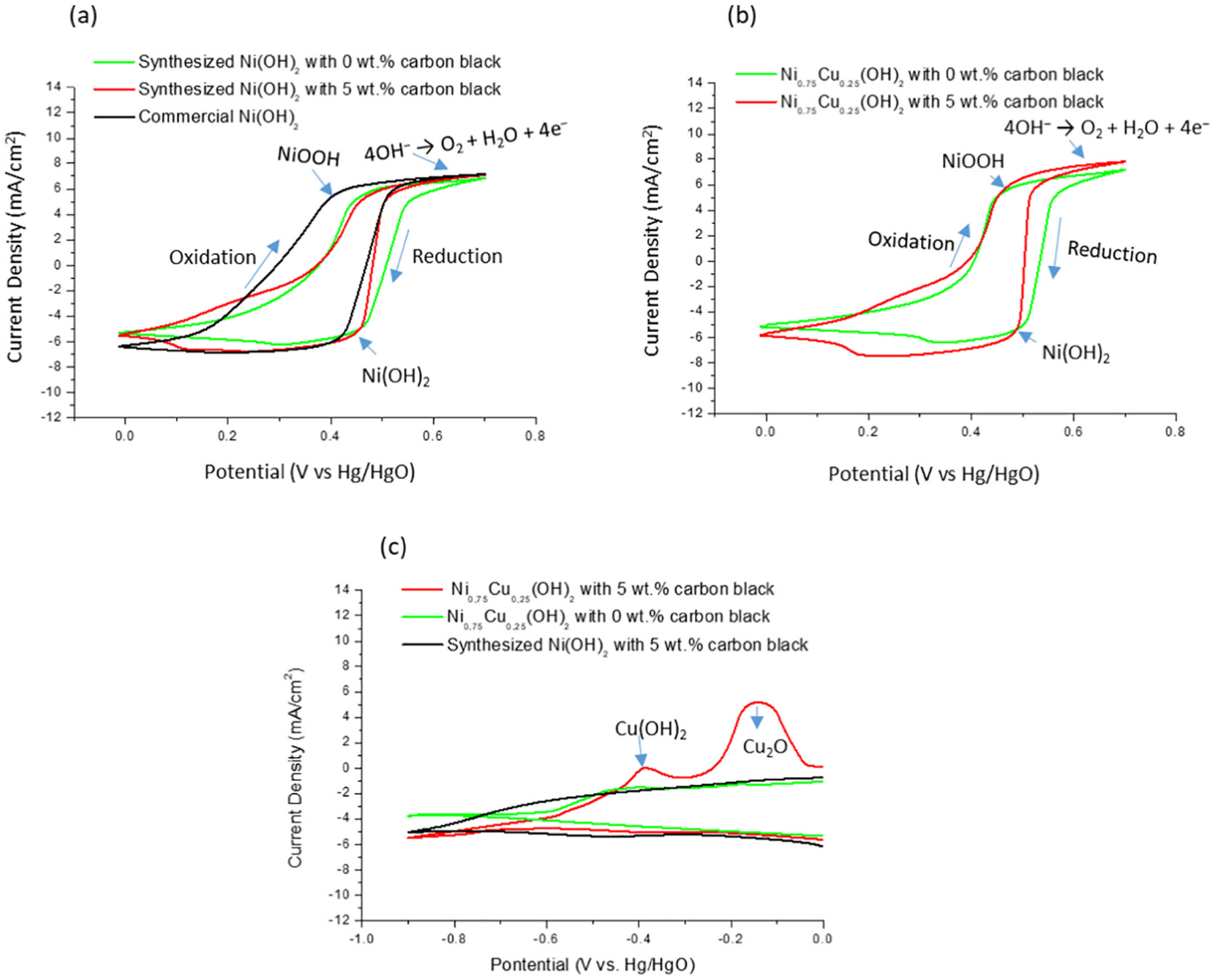

Fig. 10. Cyclic voltammograms curves of (a) Synthesized $Ni(OH)_2$ compared to commercial $Ni(OH)_2$, (b) $Ni_{0.75}Cu_{0.25}(OH)_2$ and (c) synthesized $Ni(OH)_2$ and $Ni_{0.75}Cu_{0.25}(OH)_2$ scanned at a negative potential at scanning rate of 5 mVs^{-1}.

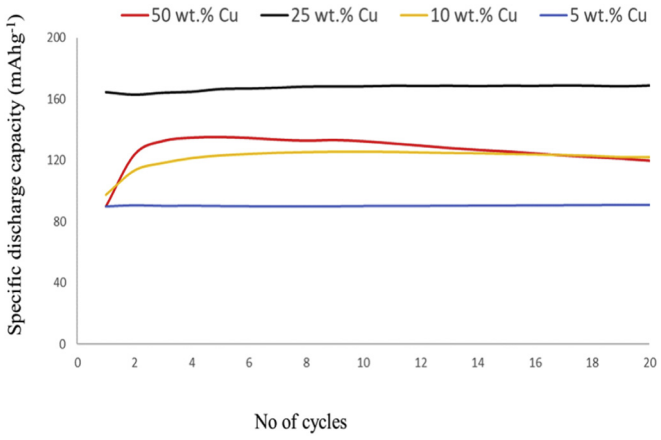

Fig. 11. Specific discharge capacity; assessing the effect of copper as a potential modifier to $Ni(OH)_2$ after the 20th cycles.

Table 5
Specific discharge capacity; assessing the effect of copper as a potential modifier to $Ni(OH)_2$ after the 20th cycles.

5 wt% Cu^{2+}	10 wt% Cu^{2+}	25 wt% Cu^{2+}	50 wt% Cu^{2+}
91 $mAhg^{-1}$	122 $mAhg^{-1}$	169 $mAhg^{-1}$	120 $mAhg^{-1}$

added. The addition of 10 wt% and 20 wt% carbon black resulted to a coulombic efficiency of 59% and 51%, respectively. The decrease in capacities may be the result of the electrode becoming too bulky, which hinders the electron transfer between active material particles and the active $Ni(OH)_2$ sites.

The same trend was observed for $Ni_{0.95}Cu_{0.05}(OH)_2$ (Table 8 and Fig. 14). Based on the obtained results it was therefore concluded that 5 wt% carbon black (85% active material and 10% binder) could be the optimum percentage needed to improve the utilization of active material in this current research.

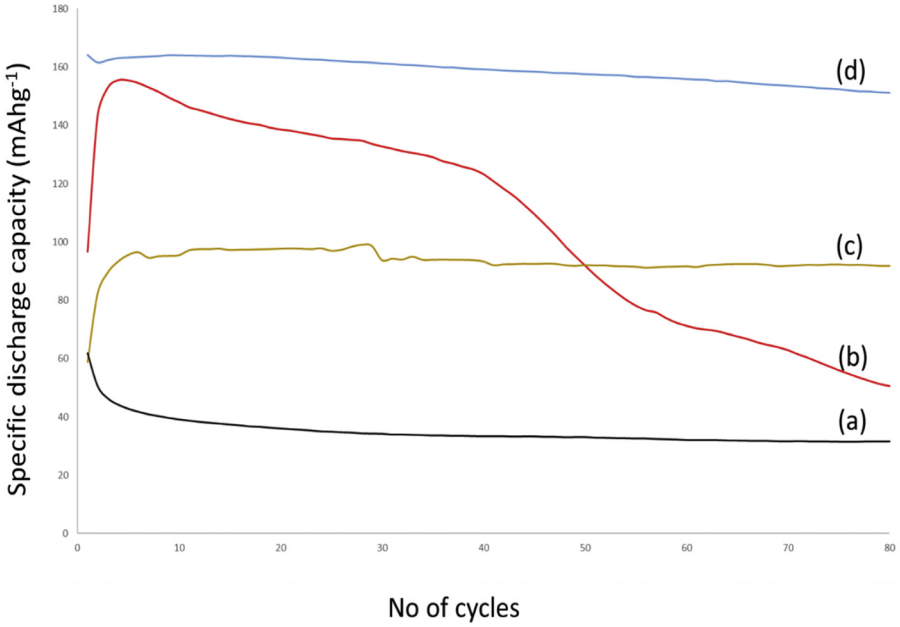

Fig. 12. Specific discharge capacities of (a) synthesized $Ni(OH)_2$ with 0 wt% carbon black, (b) synthesized $Ni(OH)_2$ with 5 wt% carbon black, (c) $Ni_{0.75}Cu_{0.25}(OH)_2$ with 5 wt % carbon black and (d) commercial $Ni(OH)_2$ over 80 cycles.

Table 6
Specific discharge capacities ($mAhg^{-1}$) of synthesized $Ni(OH)_2$ with 0 wt% carbon black, synthesized $Ni(OH)_2$ with 5 wt% carbon black, $Ni_{0.75}Cu_{0.25}(OH)_2$ with 5 wt% carbon black and commercial $Ni(OH)_2$ after various cycle numbers.

Sample name	10th	20th	30th	40th	50th	60th	70th	80th
Synthesized $Ni(OH)_2$ with 0 wt % carbon black	39	36	34	33	33	32	32	32
Synthesized $Ni(OH)_2$ with 5 wt % carbon black	148	139	133	123	92	71	63	51
$Ni_{0.75}Cu_{0.25}(OH)_2$ with 5 wt% carbon black	164	163	161	159	152	151	151	151
Commercial $Ni(OH)_2$	96	98	94	93	92	92	92	92

Table 7
Specific charge and discharge capacities in $mAhg^{-1}$ at 10 mA, 25 mA, 50 mA, and 75 mA and their coulombic efficiencies in %.

Current applied	$Ni(OH)_2$ + 5 wt% carbon black			$Ni_{0.75}Cu_{0.25}(OH)_2$ + 5 wt% carbon black		
	Specific charge capacity	Specific discharge capacity	Coulombic efficiencies	Specific charge capacity	Specific discharge capacity	Coulombic efficiencies
10	205	156	76	209	179	86
25	205	51	25	209	151	72
50	205	28	14	209	116	55
75	205	20	10	209	22	11

4. Conclusion

In this work β-$Ni(OH)_2$ and β-$Ni_{1-x}Cu_x(OH)_2$ active materials were successfully prepared by co-precipitation method followed by hydrothermal treatment. The effect of carbon black was evaluated and the CCDG results demonstrated an improved utilization of the active material when 5 wt% of carbon black was added to the electrode composition. The specific discharge capacity (after 20 cycle activation) was increased by 74% when

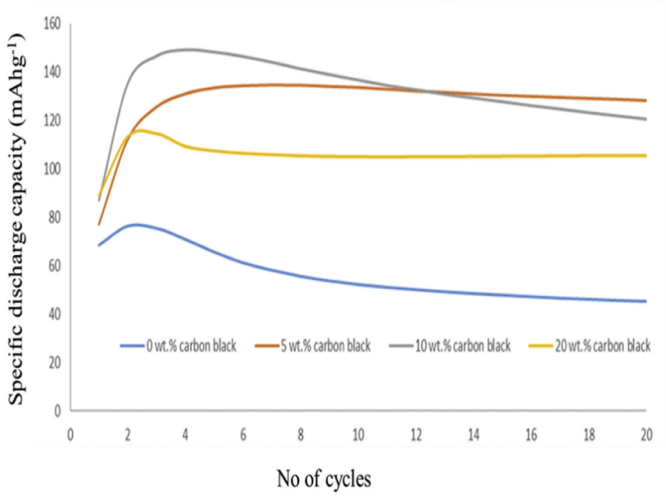

Fig. 13. Specific discharge capacity; assessing the effect of carbon black to the synthesized $Ni(OH)_2$.

compared to 0 wt% carbon black added to the nickel positive electrode. However, a drastic decrease in specific discharge capacity was observed after an additional 60 cycles. The specific discharge capacity of the synthesized $Ni(OH)_2$ with 5 wt% carbon black electrode decreased by 66% while the synthesized $Ni(OH)_2$ with 0 wt% carbon black decreased by only 18% after the 80 cycles. The addition of 25 wt% Cu^{2+} to the $Ni(OH)_2$ material resulted to an improved stability and a specific discharge capacity of 151 $mAhg^{-1}$ when compared to 51 $mAhg^{-1}$ of unmodified $Ni(OH)_2$. Unmodified $Ni(OH)_2$ has a coulombic efficiency of 25% compared to 76% for the modified $Ni(OH)_2$ after 80 cycles when a current of 25 mA was applied. Therefore the Cu^{2+} modified $Ni(OH)_2$ active material may be acknowledged as a promising material for NiFe battery positive electrode applications.

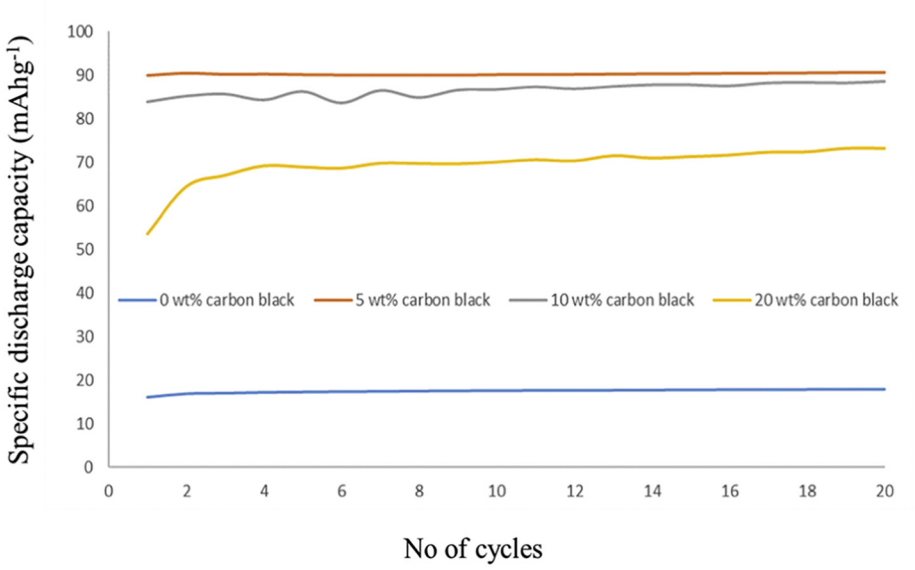

Fig. 14. Specific discharge capacity; assessing the effect of carbon black to the synthesized $NiCu(OH)_2$.

Table 8
Specific discharge capacity; assessing the effect of carbon black to the synthesized $Ni(OH)_2$ and $NiCu(OH)_2$ after the 20th cycles.

Sample name	0 wt% carbon black	5 wt% carbon black	10 wt% carbon black	20 wt% carbon black
Synthesized $Ni(OH)_2$	45mAhg^{-1}	128 mAhg^{-1}	121 mAhg^{-1}	105 mAhg^{-1}
Synthesized $NiCu(OH)_2$	18 mAhg^{-1}	91 mAhg^{-1}	89 mAhg^{-1}	73 mAhg^{-1}

Declaration of Competing Interest

The authors declare the following financial interests/personal relationships which may be considered as potential competing interests.

Acknowledgements

The authors would like to acknowledge the financial and strategic support from the Department of Science and Innovation of South Africa; Eskom Holdings SOC Ltd Reg No 2002/015527/30 (Research, Testing & Development Business Unit; and the National Research Foundation of South Africa (Grant Number: 121413).

References

[1] N. Abas, A. Kalair, N. Khan, Review of fossil fuels and future energy technologies, Futures 69 (2015) 31–49.
[2] F. Perera, Pollution from fossil-fuel combustion is the leading environmental threat to global pediatric health and equity: solutions exist, Int. J. Environ. Res. Public Health 15 (2017) 16.
[3] K. Riahi, D.P. Van Vuuren, E. Kriegler, J. Edmonds, B.C. O'neill, S. Fujimori, N. Bauer, K. Calvin, R. Dellink, O. Fricko, The shared socioeconomic pathways and their energy, land use, and greenhouse gas emissions implications: an overview, Glob. Environ. Chang. 42 (2017) 153–168.
[4] C. Oseghale, A. Abdalla, J. Posada, P. Hall, A new synthesis route for sustainable gold copper utilization in direct formic acid fuel cells, Int. J. Hydrog. Energy 41 (2016) 16394–16401.
[5] R. Sarrias-Mena, L.M. Fernández-Ramírez, C.A. García-Vázquez, F. Jurado, Improving grid integration of wind turbines by using secondary batteries, Renew. Sust. Energ. Rev. 34 (2014) 194–207.
[6] P. Warren, A review of demand-side management policy in the UK, Renew. Sust. Energ. Rev. 29 (2014) 941–951.
[7] P. Nejat, F. Jomehzadeh, M.M. Taheri, M. Gohari, M.Z.A. Majid, A global review of energy consumption, CO_2 emissions and policy in the residential sector (with an overview of the top ten CO_2 emitting countries), Renew. Sust. Energ. Rev. 43 (2015) 843–862.
[8] J.O.G. Posada, P.J. Hall, Towards the development of safe and commercially viable nickel–iron batteries: improvements to Coulombic efficiency at high iron sulphide electrode formulations, J. Appl. Electrochem. 46 (2016) 451–458.
[9] A.H. Abdalla, C.I. Oseghale, J.O.G. Posada, P.J. Hall, Rechargeable nickel–iron batteries for large-scale energy storage, Institution of Engineering and Technology Renewable Power Generation, vol. 10, 2016, pp. 1529–1534.
[10] W. Chen, Y. Jin, J. Zhao, N. Liu, Y. Cui, Nickel-hydrogen batteries for large-scale energy storage, Proc. Natl. Acad. Sci. 115 (2018) 11694–11699.
[11] S.N. Begum, V. Muralidharan, C.A. Basha, The influences of some additives on electrochemical behaviour of nickel electrodes, Int. J. Hydrog. Energy 34 (2009) 1548–1555.
[12] D.S. Hall, D.J. Lockwood, C. Bock, B.R. MacDougall, Nickel hydroxides and related materials: a review of their structures, synthesis and properties, Proce. Royal Soc. A: Math, Phys. Eng. Sci. 471 (2015) 20140792.
[13] A.S. Adekunle, J.A. Oyekunle, O. Oluwafem, A.O. Joshua, A.O. Makinde, A.O. Ogunfowokan, M.A. Eleruja, E.E. Ebenso, Comparative catalytic properties of $Ni(OH)_2$ and NiO nanoparticles towards the degradation of nitrite (NO_2^-) and nitric oxide (NO), Int. J. Electrochem. Sci. 9 (2014) 3008–3021.
[14] A.N. Kumar, S. Harish, J. Joseph, New route for synthesis of electrocatalytic $Ni(OH)_2$ modified electrodes—electrooxidation of borohydride as probe reaction, Bull. Mater. Sci. 37 (2014) 635–641.
[15] Z. Jin, P. Li, Y. Jin, D. Xiao, Superficial-defect engineered nickel/iron oxide nanocrystals enable high-efficient flexible fiber battery, Energy Storage Mater. 13 (2018) 160–167.
[16] N. Kumar, H. Panda, Facile synthesis of amorphous Co/Ni hydroxide hierarchical films and the study of their morphology and electrochemical properties, Royal Soc. Chem. Adv. 5 (2015) 25676–25683.
[17] K.-H. Young, L. Wang, S. Yan, X. Liao, T. Meng, H. Shen, W. Mays, Fabrications of high-capacity alpha-$Ni(OH)_2$, Batteries 3 (2017) 6.
[18] J.M. Gonçalves, K.M. Alves, M.F. Gonzalez-Huila, A. Duarte, P.R. Martins, K. Araki, Unexpected stabilization of α-Ni $(OH)_2$ nanoparticles in GO Nanocomposites, J. Nanomater. 2018 (2018) 13.
[19] L. Liu, Y. Hou, Y. Gao, N. Yang, J. Liu, X. Wang, Co doped α-Ni $(OH)_2$ multiple-dimensional structure electrode material, Electrochim. Acta 295 (2019) 340–346.
[20] K.H. Kim, M. Mikami, Y. Abe, M. Kawamura, T. Kiba, Structural and electrochemical properties of nanolayer-stacking structured copper-doped nickel hydroxide, Int. J. Electrochem. Sci. 13 (2018) 7655–7662.
[21] N.A. Alhebshi, H.N. Alshareef, Ternary Ni–Cu–OH and Ni–Co–OH electrodes for electrochemical energy storage, Mater. Renewable Sustain. Energy 4 (2015) 21.
[22] S.D. Giri, A. Sarkar, Electrochemical study of bulk and monolayer copper in alkaline solution, J. Electrochem. Soc. 163 (2016) H252–H259.
[23] W. Xu, R. Lan, D. Du, J. Humphreys, M. Walker, Z. Wu, H. Wang, S. Tao, Directly growing hierarchical nickel-copper hydroxide nanowires on carbon fibre cloth for efficient electrooxidation of ammonia, Appl. Catal. B Environ. 218 (2017) 470–479.
[24] A. Lassoued, M.S. Lassoued, F. Karolak, S. García-Granda, B. Dkhil, S. Ammar, A. Gadri, Synthesis, structural, optical, morphological and magnetic characterization of copper substituted nickel ferrite ($Cu_xNi_{1-x}Fe_2O_4$) through co-precipitation method, J. Mater. Sci. Mater. Electron. 28 (2017) 18480–18488.
[25] K. Young, L. Wang, W. Mays, B. Reichman, H. Chao-Ian, D. Wong, and J. Nei, "Nickel hydroxide positive electrode for alkaline rechargeable battery," ed: Google Patents, 2018.
[26] H. Wang, Y. Liang, M. Gong, Y. Li, W. Chang, T. Mefford, J. Zhou, J. Wang, T. Regier, F. Wei, An ultrafast nickel–iron battery from strongly coupled inorganic nanoparticle/nanocarbon hybrid materials, Nat. Commun. 3 (2012) 917.
[27] B.R. Wiston, M. Ashok, Electrochemical performance of hydrothermally synthesized flower-like α-nickel hydroxide, Vacuum 160 (2019) 12–17.

[28] B. Shanaj, X. John, Effect of calcination time on structural, optical and antimicrobial properties of nickel oxide nanoparticles, J. Theor. Comput. Sci. 3 (2016).
[29] M.K. Motlagh, A. Youzbashi, L. Sabaghzadeh, Synthesis and characterization of nickel hydroxide/oxide nanoparticles by the complexation-precipitation method, Int. J. Phys. Sci. 6 (2011) 1471–1476.
[30] Y.-Z. Su, K. Xiao, N. Li, Z.-Q. Liu, S.-Z. Qiao, Amorphous Ni (OH) 2@ three-dimensional Ni core–shell nanostructures for high capacitance pseudocapacitors and asymmetric supercapacitors, J. Mater. Chem. A 2 (2014) 13845–13853.
[31] V. Kovalenko, V. Kotok, A. Sykchin, I. Mudryi, B. Ananchenko, A. Burkov, V. Sololvov, S. Deabate, A. Mehdi, J.-L. Bantignies, Nickel hydroxide obtained by high-temperature two-step synthesis as an effective material for supercapacitor applications, J. Solid State Electrochem. 21 (2017) 683–691.
[32] Z. Zhai, Q. Liu, Y. Zhu, J. Cao, S. Shi, Synthesis of Ni (OH) 2/graphene composite with enhanced electrochemical property by stirring solvothermal method, J. Alloys Compd. 775 (2019) 1316–1323.
[33] H. Du, Y. Wang, H. Yuan, L. Jiao, Facile synthesis and high capacitive performance of 3D hierarchical Ni (OH) 2 microspheres, Electrochim. Acta 196 (2016) 84–91.
[34] S.A. Abbas, M.I. Iqbal, S.-H. Kim, H.A. Khan, K.-D. Jung, Facile synthesis of alfa-nickel hydroxide by an ultrasound-assisted method and its application in energy storage devices, Appl. Surf. Sci. 474 (2019) 218–226.
[35] J. Yu, S. Pan, Y. Zhang, Q. Liu, B. Li, Facile synthesis of monodispersed α-Ni (OH) 2 microspheres assembled by ultrathin nanosheets and its performance for oxygen evolution reduction, Front. Mater. 6 (2019) 124.
[36] Y. Zheng, B. Zhu, H. Chen, W. You, C. Jiang, J. Yu, Hierarchical flower-like nickel (II) oxide microspheres with high adsorption capacity of Congo red in water, J. Colloid Interface Sci. 504 (2017) 688–696.
[37] C. Coudun, F. Grillon, J.-F. Hochepied, Surfactant effects on pH-controlled synthesis of nickel hydroxides, Colloids Surf. A Physicochem. Eng. Asp. 280 (2006) 23–31.
[38] N. Kozai, H. Mitamura, H. Fukuyama, F. Esaka, S. Komarneni, Synthesis and characterization of nickel–copper hydroxide acetate, $NiCu(OH)_{3.1}(OCOCH_3)_{0.9}.0.9H_2O$, Microporous Mesoporous Mater. 89 (2006) 123–131.